Delft University of Technology

Testing of a Composite Conical-Cylindrical Shell

Rudd, Michelle Tillotson; Schultz, Marc R.; Gardner, Nathaniel W.; Kosztowny, Cyrus J. R. ; Bisagni, C.

Important note
To cite this publication, please use the final published version (if applicable).
Please check the document version above.

Testing of a Composite Conical-Cylindrical Shell

Michelle Tillotson Rudd[1]
NASA Marshall Space Flight Center, Huntsville, AL, 35812

Marc R. Schultz[2], Nathaniel W. Gardner[3], and Cyrus J. R. Kosztowny[4]
NASA Langley Research Center, Hampton, VA 23681

Chiara Bisagni[5]
Delft University of Technology, Delft, 2629HS, Netherlands

Launch-vehicle shell structures, which can be comprised of both cylindrical and conical sections, are known to be susceptible to buckling due to their large radius-to-thickness ratios. The advancements in composite manufacturing and numerical methods have enabled designers to consider more nontraditional shapes, such as connecting the conical and cylindrical sections with a toroidal transition to create a single-piece conical-cylindrical shell. This single-piece construction eliminates the need for a heavy interface ring between sections and has the potential to save mass. To better understand the buckling behavior, a composite conical-cylindrical shell was designed, fabricated, and tested. Prior to test, a finite element model that included thickness variations and radial imperfections was created. The test article buckled elastically at 251.8 kN, approximately 8.8% higher than the predicted buckling load of 231.4 kN Continued research in conical-cylindrical structures has the potential to expand the design space for launch-vehicle structures and lead to improved designs and reduced weight.

I.   Nomenclature

3CHELL	=	Composite conical-cylindrical shell test article
AFP	=	Advanced fiber placement
DIC	=	Digital image correlation
dX	=	Relative displacement in the X direction
dY	=	Relative displacement in the Y direction
dZ	=	Relative displacement in the Z direction
f	=	natural frequency
FEM	=	Finite element model
IML	=	Inner mold line
LVDT	=	Linear variable displacement transducer
MSFC	=	Marshall Space Flight Center
OML	=	Outer mold line
SLS	=	Space Launch System
Sylda	=	Système de Lancement Double Ariane

[1] Aerospace Engineer, Structural Design, Development, and Analysis Branch.
[2] Supervisory Research Aerospace Engineer, Structural Mechanics & Concepts Branch, AIAA Associate Fellow.
[3] Research Aerospace Engineer, Structural Dynamics Branch.
[4] Research Aerospace Engineer, Structural Mechanics & Concepts Branch.
[5]-Professor, Faculty of Aerospace Engineering, Kluyverweg 1, AIAA Fellow.

r	=	Radius
s	=	Longitudinal surface coordinate on a flattened cone
USA	=	Universal Stage Adapter
X	=	Positive towards 3CHELL 0-degree circumferential location
Y	=	Positive towards 3CHELL 90-degree circumferential location
Z	=	Along the axis of rotation of 3CHELL
A	=	Rayleigh mass proportional damping
B	=	Rayleigh stiffness proportional damping
α	=	Semi-vertex angle
β	=	Circumferential surface coordinate on a flattened cone
ξ	=	Damping coefficient
φ	=	Nominal fiber angle
θ	=	Circumferential location

II. Introduction

Conical and cylindrical shells are a common geometric configuration in launch vehicles. The cylindrical shape is a main component of launch vehicles due to its high strength-to-volume ratio. Conical sections are utilized when transitioning from different-diameter cylindrical components such as the transition between first and second stages, as in the Launch Vehicle Stage Adapter on NASA's Space Launch System (SLS) [1], Figure 1. Buckling is one of the failure modes that dictates the design of thin-walled primary shell structures in launch vehicles. This is due in part to the high-axial compressive loads the launch vehicle is required to support during lift-off. The same design requirements may also apply to payload adapters. The buckling of composite cylinders and cones has been investigated for current aerospace applications [e.g., 2-8].
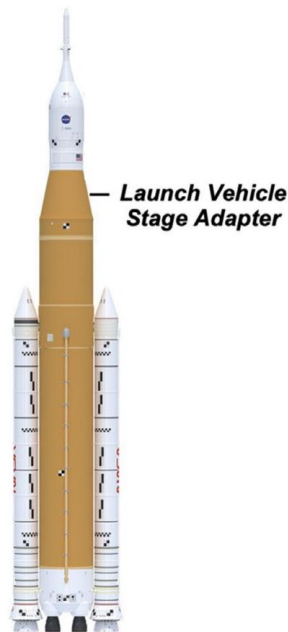

Figure 1. NASA SLS Block 1 configuration.

Designs for traditional manufacturing methods typically use heavy circumferential rings to join conical and cylindrical structures. Advances in composite manufacturing, such as advanced fiber placement (AFP) robots, and numerical tools, such as finite element codes, enable aerospace engineers to consider alternative designs with more nontraditional shapes. These shapes may include combining the conical and cylindrical components to create a conical-cylindrical shell with a toroidal transition for launch-vehicle structures. This new configuration would eliminate the need for interface rings, which can potentially lead to significant mass savings. Examples of this unique single-piece construction are the SLS Universal Stage Adapter (USA), which is currently under development [9], Figure 2, the Système de Lancement Double Ariane (Sylda) on the Ariane 5, and Vega Secondary Payload Adapter [10].

2

Figure 2. NASA's Universal Stage Adapter.

The buckling behavior of conical-cylindrical shells has been studied by several researchers using numerical and semi-analytical methods, which are mainly applicable to civil and piping applications. Anwen published a paper on the buckling of a conical-cylindrical structure with a toroidal transition segment, but assumed isotropic material properties and only considered external pressure loading [11]. Axial compression, however, is of great interest for launch vehicles. To date, Patel, et al., and Singh and Patel have published research on the buckling and postbuckling characteristics of composite conical-cylindrical shells subjected to torsion, external pressure, axial compression, and thermal loading. Their research interrogated the effects of layup, cone angle, and axisymmetric imperfections, but they did not consider a toroidal transition. In addition, the boundary conditions assumed were more in-line with the civil and piping applications [12,13]. Zarei and Rahimi published a study regarding the buckling resistance of joined composite conical-cylindrical shells, but toroidal transitions were not considered, and they focused on lateral pressure [14].

Minimal experimental data has been published for conical-cylindrical structures, and the majority of the data is related to metallic structures. Hu and Raney tested a metallic conical-cylindrical shell to validate their analytical models for vibration response rather than global buckling [15]. Bushnell and Galletly, and Zhao tested structures similar to those of Hu and Raney to failure under internal pressure to validate finite element methodologies [16,17]. In addition, the experimental research available for composite conical-cylindrical shells is not related to buckling. Mahdi, et al., studied the crushing energy absorption of cone-cylinder-cone geometry, specifically interrogating the effect of the length of the cylindrical portion on energy absorption [18]. Chronopoulos, et al., developed a numerical model to predict the broadband response of a composite conical-cylindrical shell, which was a scaled down Sylda on the Ariane 5 [19].

Not much research on the buckling behavior of composite conical-cylindrical shells for aerospace applications is reported in the literature. There is a limited amount of information published on the buckling sensitivities of this type of structure using numerical and semi-analytical techniques, and, while there is some data on metallic conical-cylindrical shells, there is no known published experimental data on the buckling of composite conical-cylindrical shells. Acknowledging the benefits of this type of structure and identifying the lack of experimental data in the current literature, a composite conical-cylindrical shell was designed, built, and tested in axial compression until buckling failure.

III.   Test Article Design and Manufacturing

A composite conical-cylindrical shell test article, referred to herein as 3CHELL, was fabricated with Hexcel IM7/8552-1[*] (190 gsm) carbon fiber epoxy system. The test-article geometry is an approximate scaled-down version of the SLS USA. The overall height of 3CHELL is 813 mm. The cylindrical inner mold line (IML) diameter is 639 mm, and the IML diameter of the top of the conical shell is 418 mm. The conical shell has a 15-degree semi-vertex angle, α. The conical shell and cylindrical shell are combined with a seamless toroidal transition with a 380 mm radius of curvature, as shown in Figure 3. The test article was designed to buckle as the critical failure mode.

---

[*]The use of trademarks or names of manufacturers in this report is for accurate reporting and does not constitute an official endorsement, either expressed or implied, of such products or manufacturers by the National Aeronautics and Space Administration.
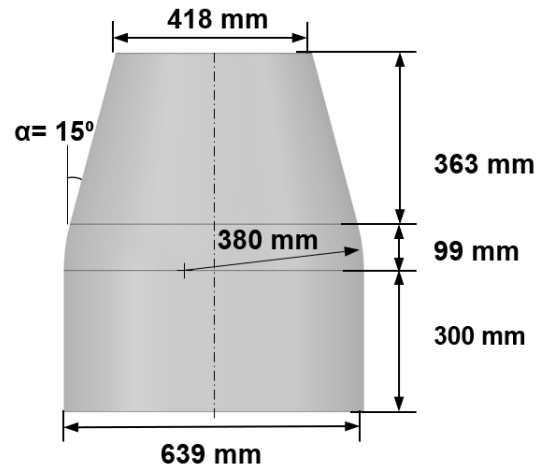
Figure 3. Test article geometry.

The test article was fabricated at the NASA Marshall Space Flight Center's (MSFC) Composite Technology Center using the advanced fiber placement (AFP) robot. Unidirectional tows, 6.35-mm wide and nominally 0.183-mm thick, were laid on an aluminum mandrel which matched the inner mold line (IML) of the test article. The selected layup is quasi-isotropic with a nominal stacking sequence of [45/-45/90/0]$_s$ with a nominal laminate thickness of 1.46 mm, where 0 degrees is parallel to the axis of rotation and 90 degrees was perpendicular. The positive ply angle is specified as clockwise from the 0-degree location when viewed from the outside. Figure 4 shows 3CHELL being manufactured at MSFC.

Figure 4. Test article being manufacture with MSFC's automated fiber placement robot.

The material properties for Hexcel IM7/8552-1 (190 gsm) were taken from data published by the National Institute for Aviation Research [20]. The lamina properties, such as elastic moduli and Poisson's ratio, are presented in Table 1. The B-basis laminate failure strength properties and laminate modulus for a layup with 25/50/25 proportion of 0-degree, 45-degree, and 90-degree plies is presented in the first two columns of Table 2. Failure strains were calculated using these values assuming a linear elastic behavior and were used to design the 3CHELL to have buckling occur prior to any strength failures under axial compression loading.

4

Table 1. Nominal lamina properties of Hexcel IM7/8552-1 composite.

0-degree modulus E_{11} (GPa)	90-degree modulus E_{22} (GPa)	Shear modulus G_{12} (GPa)	Poisson's ratio v_{12} (-)
140.9	9.72	4.69	0.356

Table 2. Documented laminate failure stresses and calculated failure strains.

Test	Failure stress (MPa)	Modulus (GPa)	Calculated failure strain (με)
Unotched tension	633.8	57.85	10,956
Unotched compression	491.3	54.19	-9065

After the test article was fabricated, it was trimmed flat and parallel to a height of 813 mm with a final trimmed weight of 3.40 kg. Following trimming, each end of the test article was potted in aluminum interface rings with 25.4 mm deep channels, which left a free length of 762 mm. The test article was centered in the end rings with a ring of epoxy potting compound 8.0 mm wide on the outer mold line (OML) and 10.9 mm wide on the inner mold line (IML). The potting rings were machined from an aluminum plate with a modulus of elasticity of 71.01 GPa and Poisson's ratio of 0.33 [21]. The epoxy potting compound had an assumed modulus of elasticity of 7.58 GPa with an assumed Poisson's ratio of 0.33 [22]. The test article potted in the end rings is shown in Figure 5.

Figure 5. Test article potted in the end rings.

IV.   Nondestructive evaluation

Thermography and structured lighting scanning were two nondestructive evaluation techniques used to assess the construction quality of the test article prior to testing. The data collect using thermography was to interrogate the integrity of the test article. The purpose of structured light scanning was to collect data on the as-built test article to better understand how radial imperfections and thickness variations affect the buckling response.

A. Thermography

The nondestructive evaluation technique of thermography was used to inspect the composite shell for flaws. From this inspection, four areas of interest were noted in the cylindrical shell. The locations and size of the indications are noted in Table 3. These areas were marked on 3CHELL to monitor during testing. Three of the four areas are located near the midheight of the cylinder, and the fourth is located near the end. No concerning areas were noted in the transition region or the conical section.

5

Table 3. Indications identified with thermography.

Indication Number	Axial Location from potted cylinder end (mm)	Circumferential Location (degrees)	Approximate size (mm)
1	193	50°	8.0 × 5.0
2	188	93°	4.3 × 4.3
3	Encased in potting	210°	2.0 × 5.8
4	203	356°	13.5 × 6.4

B. Structured Light Scanning

Once 3CHELL was potted in the aluminum interface rings, the geometry of the OML and IML was measured using structured light scanning, a photogrammetric technique as discussed in [23]. The radial imperfections of the OML and IML are shown in Figure 6a, and the thickness calculated from the OML and IML data is shown in Figure 6b. The radial imperfections of the OML and IML ranged from a maximum inward radial deviation of 0.81 mm of the nominal surface to a maximum outward radial deviation of 1.01 mm of the nominal surface. The average thickness variation in the cylindrical and transition region of the shell was 1.37 mm. This would result in an average ply thickness of 0.171 mm, which is 6.5% less than the nominal ply thickness. In the conical section, a pattern of ±45-degree thickness variations that is due to tow overlaps is apparent. The overlapped region has a maximum thickness of 1.91 mm. This pattern of overlaps can be observed in Figure 5. The pattern of overlaps is a result of the AFP process, the effort to maintain a constant angle, and the choice to eliminate gaps between each course. A tow drop occurred approximately 140 mm from the conical end, which accounts for the thickness discontinuity in the conical shell section. The thickness discontinuity is also apparent in Figure 5.
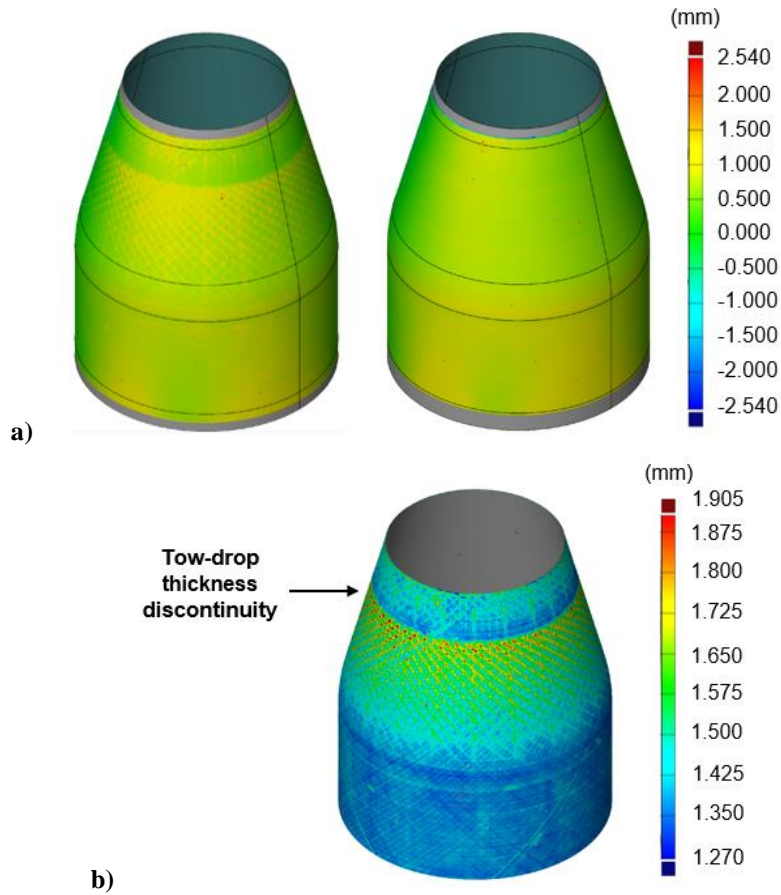

Figure 6. Structured light scan data of 3CHELL: a) radial imperfections from OML (left) and IML (right); c) measured thickness.

V.   Experimental Setup

The main objective for the test was to capture the structural response, especially the buckling behavior, of a composite conical-cylindrical shell under axial compression. To achieve this, test article 3CHELL was highly instrumented and underwent a couple of subcritical load sequences prior to the final load sequence to failure. Two subcritical load sequences, in which the load frame was used to apply axial loads up to two different load levels, both below expected failure loads. These subcritical loads were 20% and 40% of the 276.0-kN predicted geometrically nonlinear buckling load of the nominal test article. The final load case was to load 3CHELL to (buckling) failure. Testing was performed at MSFC using a load frame which is capable of applying up to 1112 kN. A nominal displacement-controlled compression rate of 0.076 mm/min was used for all load sequences. Numerous data-collection sensors such as strain gages, linear variable differential transducers (LVDTs), and low-speed and high-speed digital image correlation (DIC) systems were used to monitor the test articles prebuckling, buckling, and postbuckling response throughout all load sequences. An overview of the test setup and a closeup-view of 3CHELL in the load frame can be seen in Figure 7.
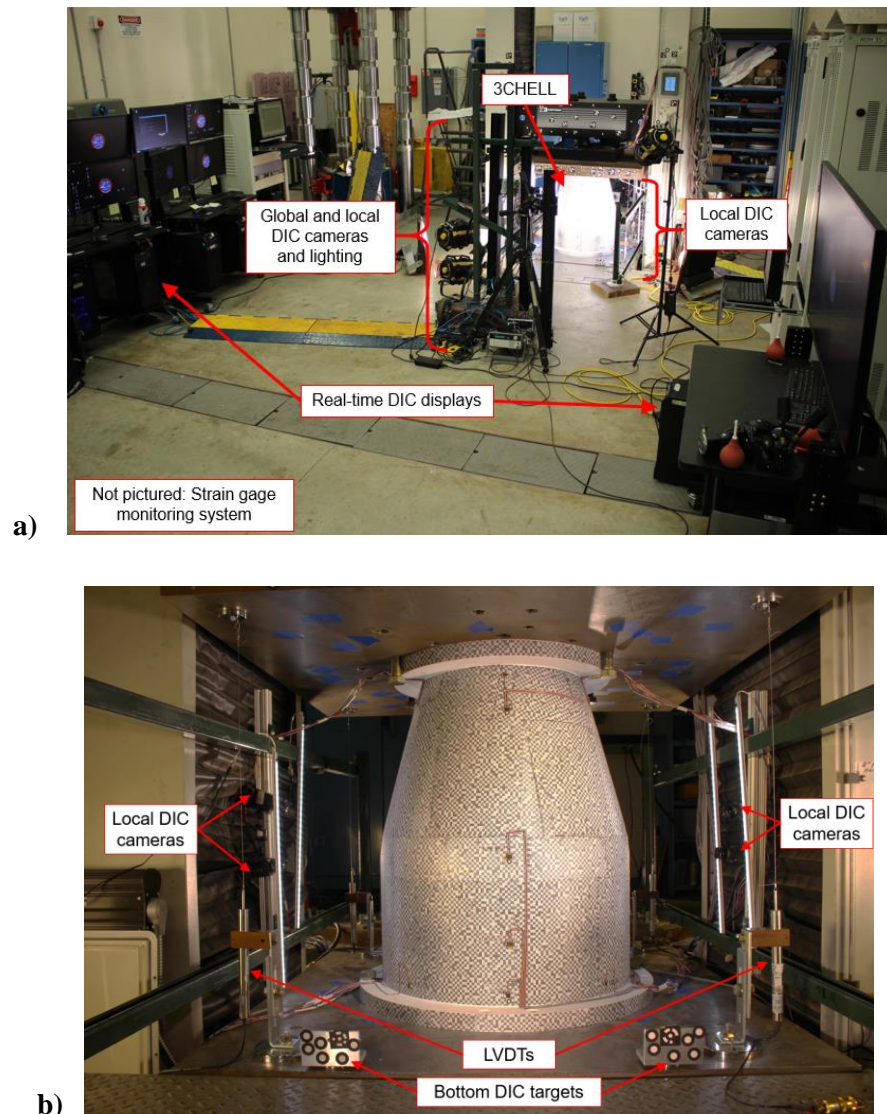

Figure 7. Test setup of 3CHELL: a) Overview of test setup.;
b) Closeup-view of 3CHELL in load frame.

7

Strain gage data was used to monitor behavior of the test article in real-time and was used for postprocessing. A series of 16 IML and 16 OML uniaxial strain gages, measuring axial strain, were placed back-to-back and spaced every 45 degrees. Half of those strain gages were located 25.4 mm from the top end ring, and the remaining half were positioned 25.4 mm from bottom end ring. In addition, 24 back-to-back biaxial gages, measuring axial and hoop strain, were placed every 90 degrees at three different axial positions. The first set of biaxial gages were placed at the midheight of the cylindrical section, the second were placed at the center of the transition region, and the third were placed just above the tow drop in the conical section. A schematic of the strain gage layout is presented in Figure 8.
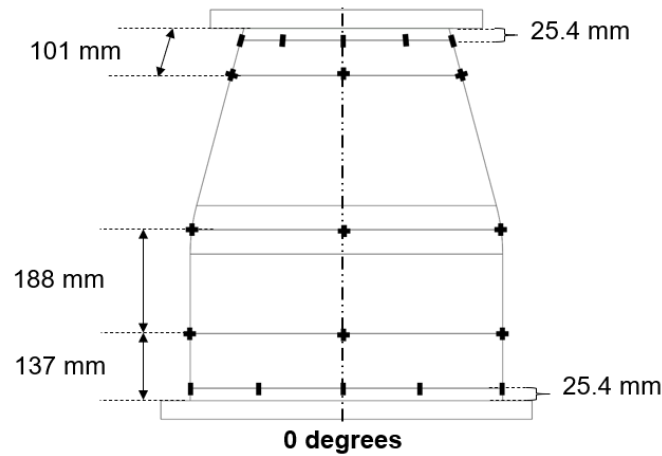

Figure 8. Strain gage layout.

Six pairs of low-speed DIC cameras (six low-speed DIC systems) and two pairs of high-speed DIC cameras (two high-speed DIC systems) were used to capture full-field displacements and strains. Of the low-speed DIC systems, the two systems centered about 0 and 180 degrees used to measure on the global behavior. Global refers to a field-of-view, approximately 711 mm x 864 mm, that includes the entire test article and end rings. The low-speed cameras had a capture rate of 1 Hz. The high-speed systems were also placed at 0 and 180 degrees with a similar global field-of-view and a frame rate of 10,000 Hz. The high-speed cameras were intended to capture the entire buckling event from just before buckling initiates throughout buckling propagation and postbuckling. The system was triggered by an operator when buckling was observed either audibly or visually and the images from when the system was triggered to approximately 2.5 seconds before the trigger was saved. It was anticipated that the buckling event would occur within this window.

Based on results produced by the finite element model with perfect geometry, high strain gradients are expected at the transition region. Therefore, four local systems were set up at 0, 90, 180, and 270 degrees with a field of view to focus on the transition region between the conical and cylindrical section. The fields of view of the local systems were approximately 297 mm x 365 mm. The local systems provided a higher resolution to measure the deformations and strains more accurately in this area of interest. The low-speed and high-speed global and local DIC camera layout is shown in Figure 9.
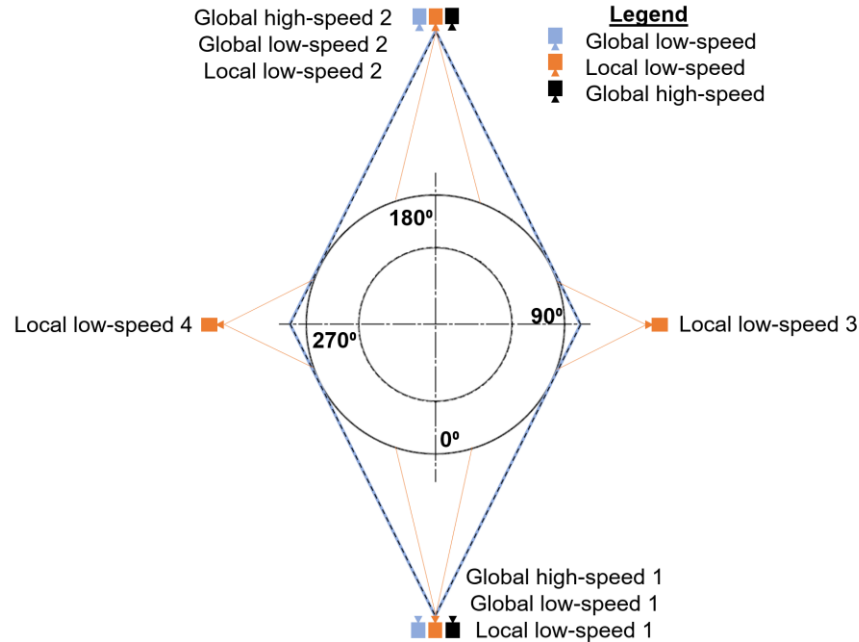
8

Figure 9. Top-down view of the DIC camera layout with approximate fields-of view.

The high-contrast speckle pattern for DIC accommodated both the low-speed (global and local) and the high-speed (global) photogrammetry requirements, which are based on camera resolution, acquisition rate, and field-of-view. The speckle size of 6.4 mm was utilized for the global systems, while a speckle size 1/10 of the global size was more appropriate for the local systems. To accommodate both speckle sizes in a single pattern, the entire test article was covered with a pattern similar to that shown in Figure 10, where it is seen that there is a two-tiered speckle pattern. The larger squares represent the speckle pattern that was utilized by the global systems, and the smaller squares within the larger squares represent the speckle patter that was utilized by the local systems. The pattern was printed on transfer paper then applied to the test article. This technique was first demonstrated by Bomarito, et al. [24, 25] on small specimens, and has also been applied to large-scale buckling test [26].
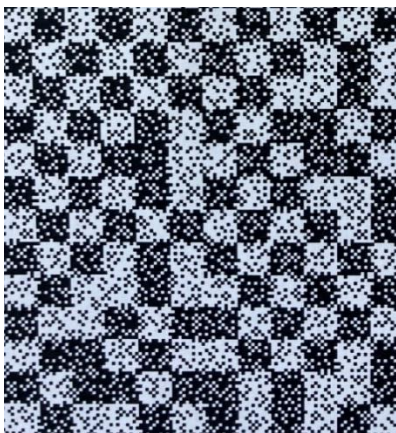

Figure 10. Example of the DIC speckle pattern for 3CHELL.

Four LVDTs were placed at the four corners of the load frame to measure relative axial displacement of the loading platens. To measure movement perpendicular to the loading direction, four targets were placed on the top and bottom corners of the load platens. These targets were monitored by a ninth DIC system to measure the movement of these points and can be seen in Figure 7.

VI. Results and Discussion

In this section a description of the finite element model (FEM) used to predict the buckling response of 3CHELL is presented. It is then followed by a comparison of the test data to the predicted response. Finally, a discussion of the off-nominal loading observed during the test, and how this anomaly affected the predicated response is presented.

A. Finite element model and analysis

A finite element model (FEM) of 3CHELL was created using Abaqus 2021 [27]. The four-node, reduced-integration shell element, S4R, was selected to characterize the solid laminate, potting compound, and end rings. A mesh convergence study was used to determine that a 5-mm mesh size was appropriate to capture the buckling behavior of the composite conical-cylindrical test article with perfect geometry. Although, a mesh size of 3.8 mm was utilized herein because the smaller mesh was necessary to incorporate the thickness variations, which were incorporated into the FEM manually.

To discretely model the thickness variations, Equation 1 [28], the equation of the fiber path for a constant angle on a conical surface was used. In Equation 1, β is the circumferential coordinate on a flattened cone, ϕ is the nominal fiber angle, s_0 is the distance from the conical apex to the top edge of the cone, s is the longitudinal surface coordinate on a flattened cone. The radius, r, is also needed for Equation 1. The flattened cone configuration and variables associated with Equation 1 is presented in Figure 11.

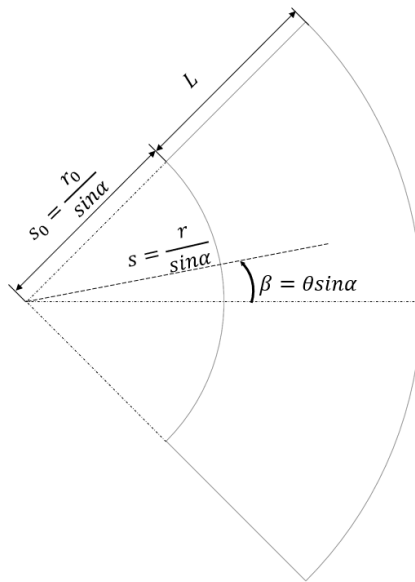$$\beta(s) = \tan\phi \ln\left[\frac{s}{s_0}\right] + \beta_0 \qquad (1)$$

Figure 11. Flatten cone configuration.

The finite element model with a detailed view of the thickness variations is presented in Figure 12. The cyan color represents the acreage or nominal layup, the light gray areas represent the end regions that are surrounded by the potting compound and end rings, the red color represents where two +45-degree plies overlap, the yellow region is where two -45-degree plies overlap, and the dark blue region is where the overlapped positive and negative 45-degree tows intersect. The positive X-axis of the FEM aligns with the 0-degree circumferential location, the positive Y-axis aligns with the 90-degree circumferential location, and Z is defined along the axis of rotation.

During manufacture, the amount of overlap in the overlapped +45 and -45 plies grew monotonically as the diameter decreased until the point where entire tows were overlapped and a tow drop was instituted. The decision to section the overlapped area in the FEM into thirds (expanded section of Figure 12) was based on calculations comparing the density of various axial sections. The stacking sequences for the composite shell are located in Table 4, where the emboldened font indicates an overlapped ply. The IML structured light scan data was used as the radial imperfections for the FEM since the OML data has influences of the thickness variations. The process in which the radial imperfections were incorporated is explained by Kosztowny [29]. In addition, the measurement-derived average ply thickness of 0.171 mm was used.
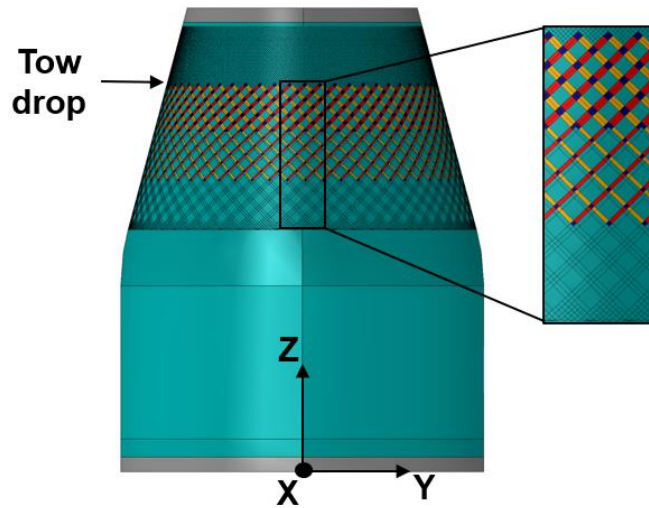
10

Figure 12. Finite element model with thickness variation details.

Table 4. FEM Section Properties.

Section	FEM color	Stacking Sequence
Acreage	Cyan	45/-45/90/0/0/90/-45/45
+45 overlap	Red	45/**45**/-45/90/0/0/90/-45/**45**/45
-45 overlap	Yellow	45/-45/**-45**/90/0/0/90/**-45**/-45/45
+45 and -45 overlap	Dark blue	45/**45**/-45/**-45**/90/0/0/90/**-45**/-45/**45**/45
Potted ends	Gray	Al ring/Potting/Acreage/Potting/Al ring

The end-ring configuration in the test article approximates a clamped boundary condition. To apply clamped boundary conditions in the FEM, reference points were placed on the axis of rotation at the top and bottom. Tie constraints were used to connect all degrees of freedom to the respective reference points at the top and bottom ends of the shell. The bottom reference point had all degrees of freedom fixed, and the top reference point had all degrees of freedom fixed except for axial displacement.

Using these analysis parameters, linear eigenvalue and implicit nonlinear transient analyses were used to predict the structural response of 3CHELL. The Lanczos solver was used to determine the linear buckling loads and modes. To determine the damping parameters (the Rayleigh mass proportional damping, A, and the Rayleigh stiffness proportional damping, B) for the nonlinear transient analysis, the first natural frequency, *f*, from a free vibration analysis was required. The equations for Rayleigh mass and stiffness proportional damping constants were calculated using Equations 2 and 3, where the damping coefficient, ξ, of 0.05 was assumed.

$$A=2\pi f\xi \tag{2}$$

$$B=\frac{\xi}{2\pi f} \tag{3}$$

The transient dynamic analysis used a time duration of 2000 seconds. An applied displacement was ramped linearly from 0.00 mm to -2.54 mm at the top reference node to obtain the load rate of 0.076 mm/min that was used in the test. This was completed in a single step in the analysis. The time integrator parameter, alpha, of -0.05 was used for slight numerical damping as suggested by Reference [27]. The half increment solution parameter was set equal to the approximate buckling load of 3CHELL.

B. Test-analysis correlation

The test article 3CHELL buckled at a load of 251.8 kN, 7.1% greater than the predicted buckling load of 235.1 kN. The load versus displacement curves for the predicted and measured behavior are in Figure 13. The end shortening data was determined using DIC by measuring the change in length between a point on the top and bottom ring. It is observed that the test article was approximately 14% stiffer than the FEM. The change in slope that occurs at approximately 50 kN is believed to when uniform load introduction was achieved.

The predicted radial displacements at incipient buckling are presented in Figure 14a. Multiple potential buckling initiation sites can be observed as blue and black dimples just above the transition region with a maximum inward displacement of -0.42 mm. Another band of blue dimples is seen just below the transition in the cylindrical portion as well, but the maximum inward displacement in this region is only -0.08 mm. A third row of dimples, not as pronounced at the first two, is observed just above the tow drop region. Ultimately, it was predicted that buckling would initiate with the dimple located at the 120-degree circumferential location in the cone just above the transition region. The outward radial displacements were predicted to be relatively consistent with the most pronounced outward deformations shown in Figure 14a as two red bands in the transition region. The maximum outward radial displacement is 0.87 mm. Even with the presence of radial imperfections, the radial displacements are relatively uniform at a given longitudinal location, meaning that just above the tow drop around the entire circumference the radial displacement is approximately 0.27mm.

There are similarities between the predicted radial displacements, Figure 14a, and the observed radial displacements during test, Figure 14b. For example, the three sets of relatively inward radial displacements can be seen just above and below the transition region, and just above the tow drop. In addition, the region of the most outward deformation occurred in the transition region with the same magnitude that was predicted by the model of 0.87 mm.

On the other hand, while magnitude of the maximum outward displacement in the model was similar to the test, the measured maximum inward displacement incipient of buckling is approximately half of what was predicted, -0.2 mm. There were similarities in the axial location of the radial displacement patterns, but the dimples in the cylindrical region were more prominent in the test data instead of the conical region as predicted. It is also interesting to note that the radial displacements seem skewed at a given axial location while in the predictions it is uniform. This skew can be identified globally by the presence of the shades of green and light blue in the conical region in the figure centered about 0-degrees, and the dark blue and purple colors in the conical region in the figure centered about 180-degrees. More specifically, just above the tow-drop region at the 0-degree circumferential location the measured radial displacement is 0.44 mm. The measured radial displacement at 180-degrees at the same axial location is 0.13 mm.
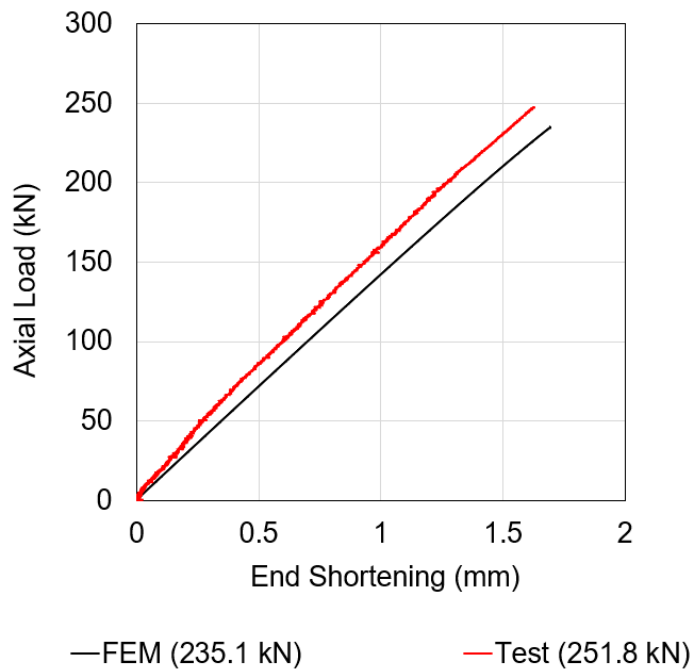

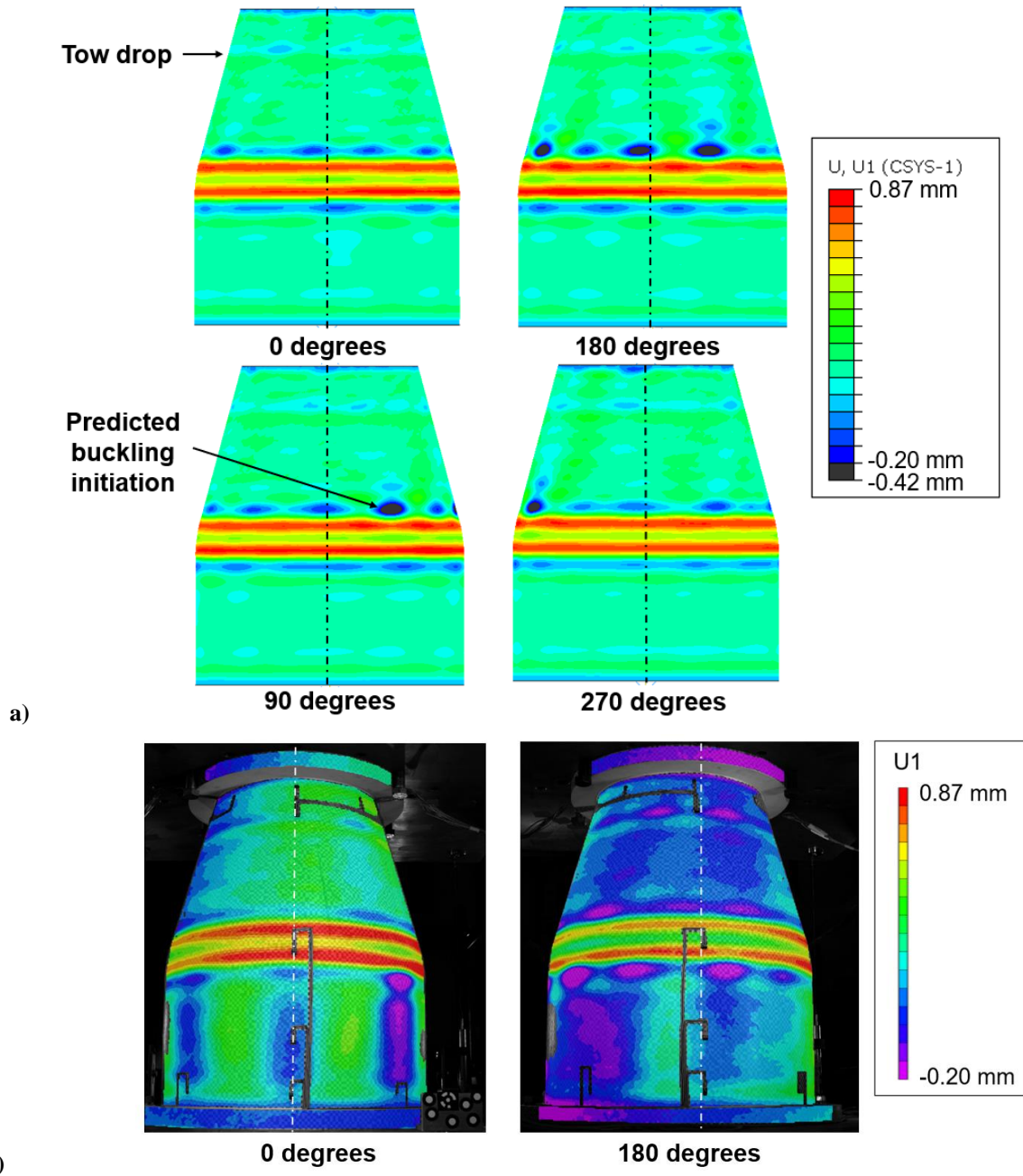**Figure 13. Axial load versus end shortening curve from the FEM and test.**

12

Figure 14. Radial displacement incipient of buckling for low-speed data: a) FEM; b) test.

It is suspected that buckling initiated in the cylinder just outside the field of view of the 180-degree-centered high-speed DIC system, which encompasses the circumferential coordinates of approximately 125 degrees to 235 degrees (Figure 15). Figure 15 shows the radial displacements from the high-speed camera from buckling initiation and 1.6 milliseconds into the buckling event. In the first high-speed image, there is a purple inward dimple that forms on the edge of the field of view, circled. Between the initial image and 1.6 milliseconds the dimple grows and begins to propagate. Figure 15c shows the postbuckling configuration with three dimples in the cylindrical section. These features can also be seen in Figure 16. The buckling event was apparently elastic, meaning no material failure or permanent deformation was observed visually, in the strain data or DIC data. This also suggests that the indications found using thermography did not adversely affect the strength of 3CHELL.
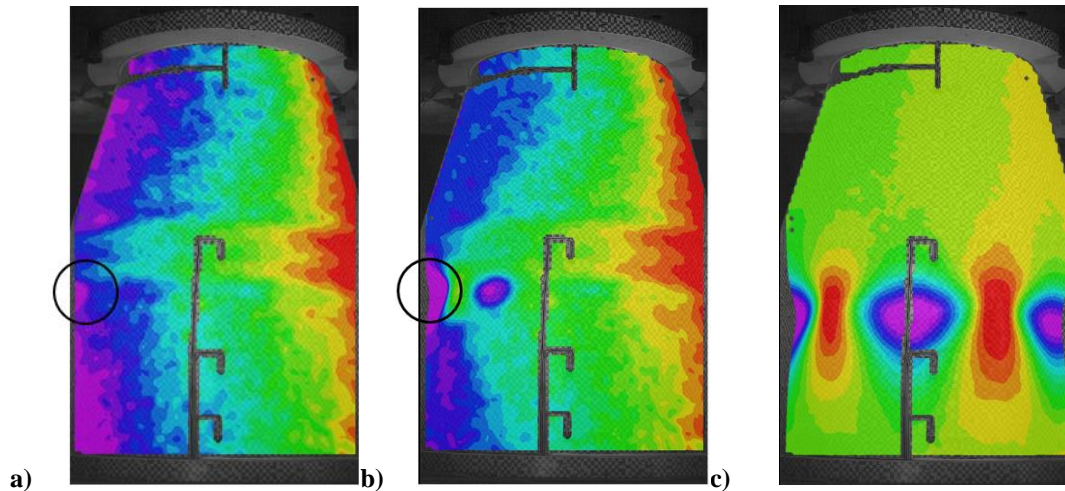
Figure 15. Radial displacement from a high-speed DIC system centered at 180 degrees: a) buckling initiation; b) 1.6 milliseconds into buckling propagation.
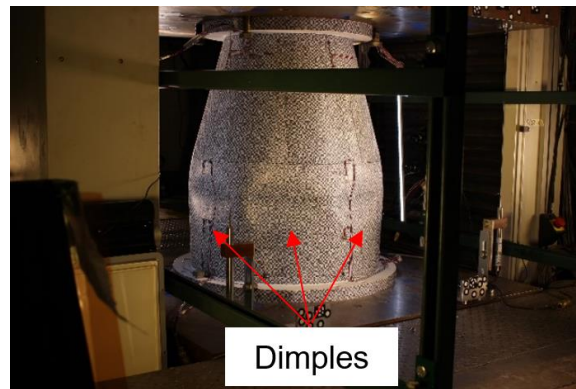

Figure 16. Postbuckling configuration of 3CHELL from the first test.

During testing, a shearing motion in the load frame was identified using real-time DIC displays, so the decision was made to measure the movement of the top and bottom load platen using a set of targets located on the top and bottom load platen in the X, Y, and Z direction. The coordinate system with respects to the load frame and the orientation of 3CHELL is shown in Figure 17. The measurement dZ is the relative change in axial position between the top and bottom load platens. The measurement dX is the relative change in lateral displacement in the X direction (toward 0 degrees). The measurement dY is the relative change in lateral displacement between the top and bottom load platens in the Y direction (toward 90 degrees). The results of the measurement of the relative motion of the platens confirmed that a shear load was being applied to the test article. The DIC-measured relative displacement between the top and bottom end rings (as opposed to the platens) in the X and Y direction is shown Figure 18. It can be observed from this figure that the relative displacement between the top and bottom end rings at buckling was 0.16 mm in the X direction and 0.31 mm in the Y direction. This displacement results in a magnitude of 0.35 mm towards the 62-degree circumferential location. The total axial displacement of the test article at buckling was 1.65 mm, so the in-plane displacement was approximately 20% of the total axial shortening.
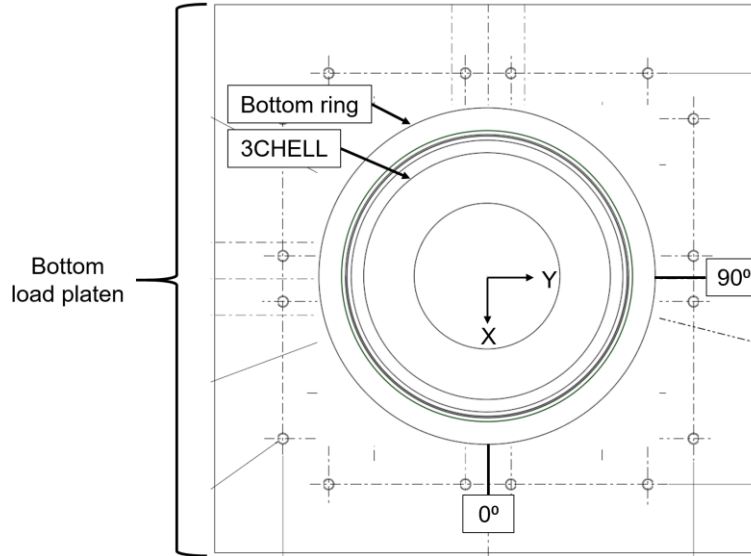
Figure 17. Top-down view of 3CHELL in load frame with coordinates for crosshead movement.
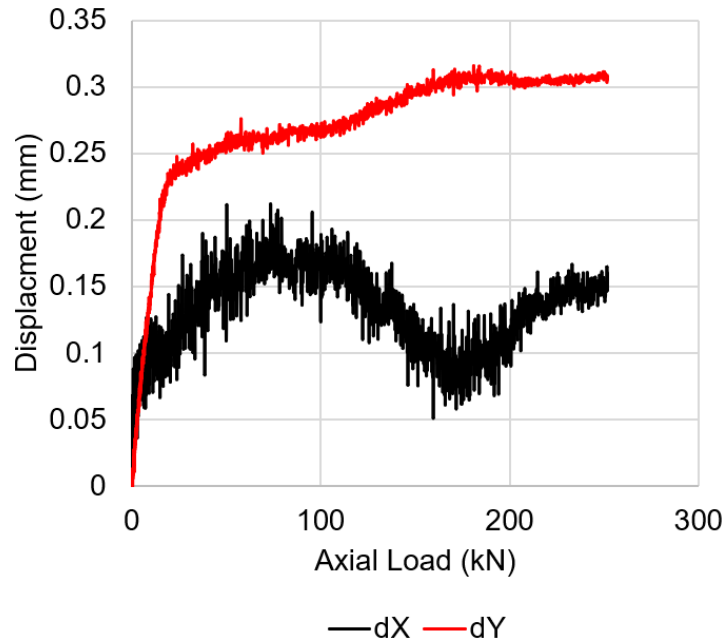

—dX —dY

Figure 18. Measured load platen movement.

To represent the measured off-nominal shear displacement in the finite element analysis, an additional step was created in the analysis. The first step was used to simulate the relative shear displacements of 0.16 mm in the X direction and 0.31 mm in the Y direction. The second step was used to simulate the application of the axial displacement at a rate of 0.076 mm/min, same as used in the initial analysis.

The predicted buckling load with the shear displacement included was 231.4 kN, which is almost 2% lower than the initial FEM prediction and 8.8% lower than the experimental buckling load. In the load-verses-displacement curves, Figure 19, it can be observed that the stiffnesses of the FEM with and without the shear displacement are indistinguishable, but that the predicted buckling load with the included shear displacement is slightly lower. While there was minimal change in the overall response, a skewed pattern in the predicted radial displacements incipient of buckling is observed in the conical region in Figure 20. The shear increased the predicted outward radial displacements to 1.0 mm, but the maximum inward radial displacement remained unchanged. The inclusion of shear did not significantly influence the results, despite the fact that the magnitude of the shear displacement was 20% of the total end shortening.

15

The differences between test and analysis may be attributable to the assumptions made when incorporating the thickness variations. The weight of the FEM was 3.31 kg and the weight of 3CHELL was 3.40 kg. It is presumed that the weight difference is because there is more material in the test article than what was modeled. This additional material is likely related to the tow overlaps which form the grid-like pattern seen in the thickness variations in Figure 6b.
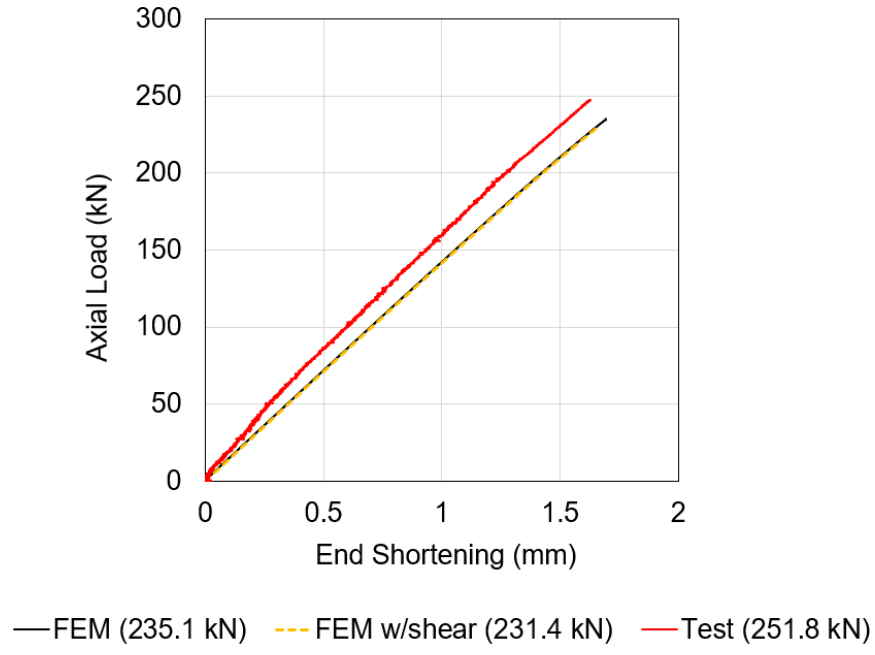

Figure 19. Axial load versus end shortening curve from the FEM with shear and without shear, and test.
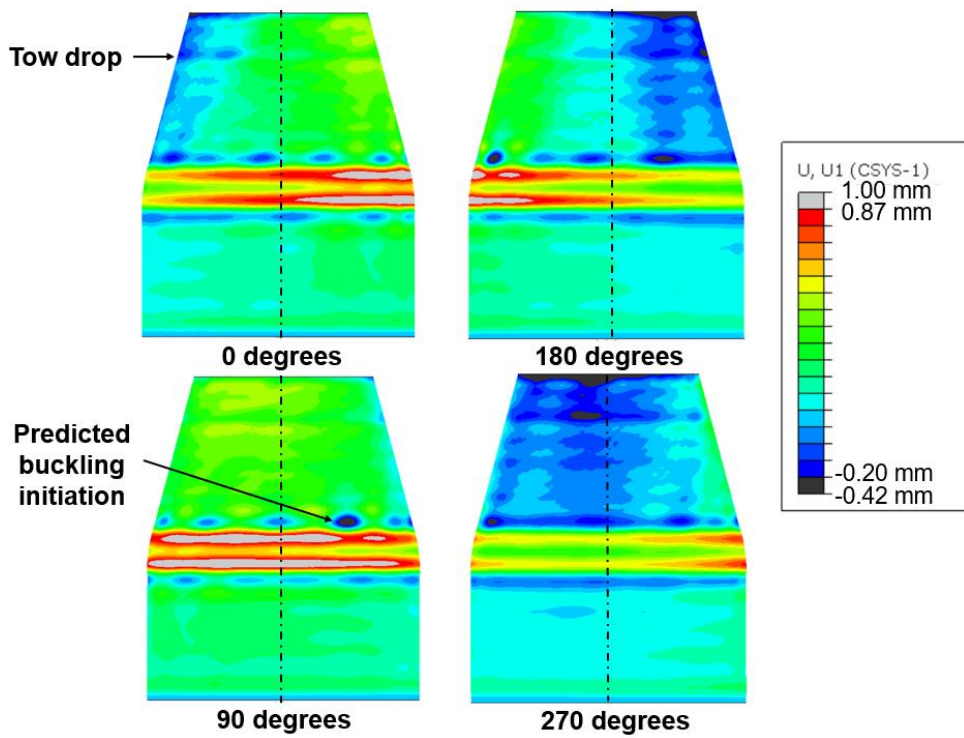

Figure 20. FEM with shear radial displacements incipient of buckling.

16

VII. Conclusions

Utilizing a single-piece composite conical-cylindrical shell with a toroidal transition for aerospace applications, for example NASA's Universal Stage Adapter, has the potential to save structural mass and expand the design space for launch vehicle and payload adapters. This geometry combines cylindrical and conical shells common in launch vehicle architecture, thereby eliminating the heavy, stiff interface ring that often separates two independent shell structures. However, such conical-cylindrical shells, as well as conical and cylindrical shell structures, are susceptible to stability failures such as global buckling due to their large radius-to-thickness ratios. A composite conical-cylindrical shell with a toroidal transition, 3CHELL, was designed to fail in buckling, fabricated, and tested in an effort develop a better understanding the buckling response of this type of shell structure. A FEM that included thickness variations and radial imperfections was developed and implicit nonlinear transient analyses were conducted to predict the structural response. The test article buckled at 251.8 kN, and the predicted buckling load from an analysis which included measured off-nominal shear movement of the load platens was 231.4 kN. The test article was also approximately 14% stiffer than the FEM. These discrepancies are possibly attributable to the assumptions made when incorporating the thickness variations.

Acknowledgments

References

[1]   National Aeronautics and Space Administration, "NASA's Space Launch System Reference Guide 2022," https://www.nasa.gov/sites/default/files/atoms/files/sls_reference_guide_2022_print_0.pdf, accessed November 2022.

[2]   Bisagni, C., "Numerical Analysis and Experimental Correlation of Composite Shell Buckling and Post-Buckling," *Composite Part B: Engineering*; Vol. 31, No.8, 2000, pp. 55–67.

[3]   Labans, E., Bisagni, C., "Buckling and Free Vibration Study of Variable and Constant Stiffness Cylindrical Shells," *Composite Structures*, Vol. 210, 2019, pp. 446–457.

[4]   Schultz, M.R., Sleight, D.W., Gardner, N.W., Rudd, M.T., Hilburger, M.W., Palm, T., Oldfield, N.J.. "Test and Analysis of a Buckling-Critical Large-Scale Sandwich Composite Cylinder." AIAA SciTech 2018 Forum, Orland, Florida; 2018. Paper number 1693.

[5]   Rudd, M.T., Schultz, M.R., Waters, W.A., Jr. Gardner, N.W., Bisagni, C., "Buckling Testing of a Subscale Composite Cylinder," *AIAA/ASME/ASCE/AHS/ASC Structures, Structural Dynamics & Materials Conference*, Virtual, January 2021, Paper number 0205.

[6]   Khakimova, R., Wilckens, D., Reichardt, J., Zimmermann, R., Degenhardt, R., "Buckling of Axially Compressed CFRP Truncated Cones: Experimental and Numerical Investigation," *Journal of Composite Structures*, Vol. 146, 2016, pp. 232-247.

[7]   Sleight, D.W., Satyanarayana, A., Li, Y., and Schultz, M.R., "Buckling Imperfection Sensitivity of Conical Sandwich Composite Structures for Launch-Vehicles," AIAA SciTech 2018 Forum Orlando, FL, January 2018, Paper number 1696.

[8]   Wagner, H. N. R., Huhne, C., Niemann, S., "Robust Knockdown Factors for the Design of Axially Loaded Cylindrical and Conical Composite Shells- Development and Validation," Journal of Composite Structures, Vol. 173, 2017, pp. 281-303.

[9]   National Aeronautics and Space Administration. "Universal Stage Adapter." https://www1.grc.nasa.gov/space/usa/, last accessed on November 2022.

[10]   European Space Agency, "Deploying Multiple Satelites with Sylad and Vespa," https://www.esa.int/Enabling_Support/Space_Transportation/Deploying_multiple_satellites_with_Sylda_and_Vespa, last accessed on November 2022.

[11]   Anwen, W., "Stresses and Stability for the Cone-Cylinder Shells with Toroidal Transition," International *Journal of Pressure Vessels and Piping*, Vol. 75, No. 1, 1998, pp. 49–56.

[12]   Patel B. P., Nath, Y., and Shukla, K.K., "Nonlinear Thermo-Elastic Buckling Characteristics of Cross-Ply Laminated Joined Conical- Cylindrical Shells," *International Journal of Solids and Structures*, Vol. 43, No. 16, 2006, pp. 4810–4829.

[13] Singh S., Patel B.P., and Nath Y., "Postbuckling Behavior of Angle-Ply Laminated Joined Circular Conical-Cylindrical Shells," *American Institute of Aeronautics and Astronautics Journal*, Vol. 45, No. 4, 2007, pp. 942–949.

[14] Zareim, M., Rahimi, G.H., "Buckling Resistance of Joined Composite Sandwich Conical-Cylindrical Shells with lattice core under lateral pressure," *Thin-Walled Structures*, Vol. 174, 2022, 109027.

[15] Hu, W. C. L., Raney, J. P., "Experimental and Analytical Study of Vibrations of Joined Shells," *AIAA Journal*, Vol. 5, No. 5, May 1967, pp. 976-980.

[16] Bushnell, D., Galletly, G.D., "Comparisons of Test and Theory for Nonsymmetric Elastic-Plastic Buckling of Shells of Revolution." *International Journal of Solids Structures*, Vol. 10, 1974, pp. 1271-1286.

[17] Zhao, Y., "Buckling Behaviour of Imperfect Ring-Stiffened Cone–Cylinder Intersections Under Internal Pressure," *International Journal of Pressure Vessels and Piping*, Vol. 82, No. 7, 2005, pp. 553–564.

[18] Mahdi, E., Hamouda, A., Sahari, B., Khalid, Y., "Crushing Behavior of Cone-Cylinder-Cone Composite System," *Mechanics of Advanced Materials and Structures*, Vol. 9, 2002, pp. 99-117.

[19] Chronopoulos, D., Ichchou, M., Troclet, B., Bareille, O., "Predicting the Broadband Response of Layered Cone-Cylinder-Cone Shell," *Journal of Composite Structures*, Vol. 107, 2014, pp. 149-159. http://dx.doi.org/10.1016/j.compstruct.2013.07.055

[20] Clarkson, E. "Hexcel 8552 IM7 Unidirectional Prepreg 190 gsm & 35%RC Qualification Statistical Analysis Report," Technical Report NCP-RP-2009-028 Rev B; 2019.

[21] Metallic Materials Properties Development and Standardization (MMPDS), vol. 10, April 2015.

[22] Micor Microrox® Standard Grout Data Sheet, https://www.micorco.com/wp-content/uploads/2014/03/Micorox-Standard-Grout-PDF-3-2014.pdf, last accessed November 2022.

[23] Alexander, B.F., Ng, K.C.. "3D. Shape Measurement by Active Triangulation Using an Array of Coded Light Stripes," *SPIE: Optics, Illumination and Image Sensing for Machine Vision II*, Vol. 850, 1988, pp. 199–209.

[24] Bomarito, G.F., Hochhalter, J.D., Ruggles, T.J., Cannon, A.H., "Increasing Acuracy and Precision of Digital Image Correlation Through Pattern Optimization," *Optics and Lasers in Engineering*, Vol. 91, 2017, pp. 73-85. https://doi.org/10.1016/j.optlaseng.2016.11.005.

[25] Bomarito, G.F., Hochhalter, J.D., Ruggles, T.J.,"Development of Optimal Multiscale Patterns for Digital Image Correlation via Local Grayscale Variation," *Experimental Mechanics*, Vol. 58, 2018, pp. 169-1180. https://doi.org/10.1117/12.942878.

[26] Song, K., Schultz, M.R., Kosztowny, C.J.R, Przekop, A., Gardner, N.W., Rudd, M.T., "Buckling Test and Analysis of the 8-foot-Diameter Sandwich Composite Cylinder Test Article CTA8.3 as Part of the Shell Buckling Knockdown Factor Project: Test Dates 16−19 December 2019," NASA/TM- 20210024768, January 2022.

[27] ABAQUS/Standard User's Manual. Version 2021 ABAQUS. Inc. USA; 2021.

[28] Blom, A.W., Tatting, B.F., Hol, J.M.A.M, Gurdal, Z., "Fiber Path Definitions for Elastically Tailored Conical Shells" *Composites Part B: Engineering*; Vol. 40, 2009, pp. 77-84.

[29] Kosztowny, C. J. R., "Implementing Geometric Surface Imperfections into Sandwich Composite Cylinder Finite Element Method Models," AIAA SciTech 2021 Forum, January 2021, VIRTUAL EVENT.